*J. Fluid Mech.* (1993), *vol.* 255, *pp.* 667–681



# A dynamical systems approach to the early stages of boundary-layer transition

By J. J. HEALEY

University of Cambridge, Department of Engineering, Trumpington Street, Cambridge CB2 1PZ, UK

(Received 12 November 1992 and in revised form 10 May 1993)

A series of experiments has been performed on a laminar flat-plate boundary layer undergoing transition to turbulence. Reproducible disturbances were introduced via a loudspeaker embedded at some upstream location. Time series of the velocity fluctuations were obtained at a sequence of downstream locations using hot-wire anemometry and the phase portraits were reconstructed at each position. A new technique has been used to estimate the number of independent modes. Nonlinear maps were then fitted that transform the portrait at one streamwise location onto the portrait at the neighbouring downstream position. In this way the spatial evolution of disturbances is modelled explicitly. These maps agree with classical linear stability theory for small disturbances, and appear to give rise to 'Smale horse-shoe'-like behaviour for larger amplitude disturbances. This may provide a mechanism for generating sensitive dependence on initial conditions, and illustrates a possible role for low-dimensional chaos in boundary-layer transition.

## 1. Introduction

The identification of coherent structures in turbulent flows and attempts to understand their evolution and interactions are currently active fields of research, see Hussain (1986). The conjecture is that certain aspects of such flows may be dominated by these structures and hence make the flow amenable to deterministic modelling. Coherent structures like hairpin vortices are generated during the transition process and so the study of transition itself may be an important step towards understanding turbulence.

In particular, this work is concerned with the transition from a laminar flow to turbulence in the boundary layer that develops over a flat plate at zero incidence to the free stream. This classical arrangement is an archetype for smooth aerofoils and so is of additional practical importance. The Tollmien–Schlichting modal selection process for infinitesimal harmonic perturbations of a steady parallel boundary layer successfully predicts the evolution of small-amplitude disturbances. For larger disturbances, however, the presence of nonlinearity becomes significant and new techniques must be developed to study the dynamical processes involved in the generation of complex fluid behaviour.

In this paper a novel method based on ideas from dynamical systems theory is presented and applied to time series obtained from experiments carried out in the low-turbulence wind tunnel in the Engineering Department of Cambridge University. Unlike previous approaches, this method incorporates an explicit spatial element into the analysis. This is essential because, in common with many shear-layer flows, the instability is *convective*, see Gaster (1962). This statement expresses the fact that at any

given measurement station the amplitude of a harmonic excitation, while constant in time, varies exponentially with position, i.e. $A \propto e^{\lambda x}$ instead of the usual $e^{\lambda t}$ (which would correspond to an *absolute* instability).

The spatial evolution is represented by a series of nonlinear maps which transform points from one reconstructed phase portrait to another taken from a different streamwise position in the boundary layer. These maps may be called 'spatial' since, under iteration, they propagate disturbances in space rather than in time. A brief account of the experiment is given in §2. The data analysis techniques are presented in §3 and examples of applications to experimental data are given in §4. The principal findings of this research are summarized in §5.

## 2. The experiment

### 2.1. *Experimental arrangement*

The experiments were carried out on a flat plate mounted vertically in the $0.914 \times 0.914$ m working section of a small closed-return wind tunnel. The wind tunnel was developed to have extremely low levels of background turbulence so that the behaviour of controlled excitations would not be masked. This was achieved through the use of a 5 mm deep paper honeycomb followed by four fine mesh screens. The r.m.s. turbulence intensity at the inlet of the working section was less than 0.01 % of the free-stream velocity, 18.0 m $s^{-1}$, within the frequency range 4–4000 Hz, see Gaster (1990). The plate and flap arrangement were set up to achieve an essentially zero pressure gradient over the region where measurements were made.

A hot-wire anemometer was mounted on a computer-controlled traversing system attached to the side panel of the tunnel, enabling three-dimensional positioning of the probe. The electrical signal generated by a DISA 55M01 constant-temperature anemometer unit was processed by a low-noise pre-amplifier and band-pass filter which admits the range 4–4000 Hz. The resulting signal was then digitized by a 12-bit A-D (analogue to digital) converter fitted with a further computer-controlled amplification stage.

The excitation of the flow was provided by a buried loudspeaker that communicated with the boundary layer via a small hole 200 mm from the leading edge on the centreline of the plate. Some noise was inevitably generated by the presence of the driving hole, but by interposing some felt material between the loudspeaker and the hole, this was reduced to an acceptable level.

Motivated by the work of Gaster (1990), an excitation signal consisting of a sine wave with added white noise was employed. The frequency of the sine wave was 200 Hz, placing it within the band of amplified Tollmien–Schlichting waves. The noise was obtained by adding computer-generated random numbers to the sine wave, and so was exactly reproducible (they were calculated using an algorithm from Press *et al.* 1986). The purpose of adding this noise was to 'drown out' the ubiquitous low-level background noise, effectively making the broadband component of the signal reproducible. This is important because Gaster (1990) demonstrated that breakdown can occur through the nonlinear coupling of the fundamental driving frequency and the broadband excitations always present.

The A-D collecting the data was phase locked with the D-A driving the loudspeaker with the computer-generated signal. A sampling frequency of 8192 Hz was used to provide approximately 40 points per cycle of the sine wave. This high sampling frequency is found to be necessary so as to obtain good phase portrait reconstructions (see §3.1).

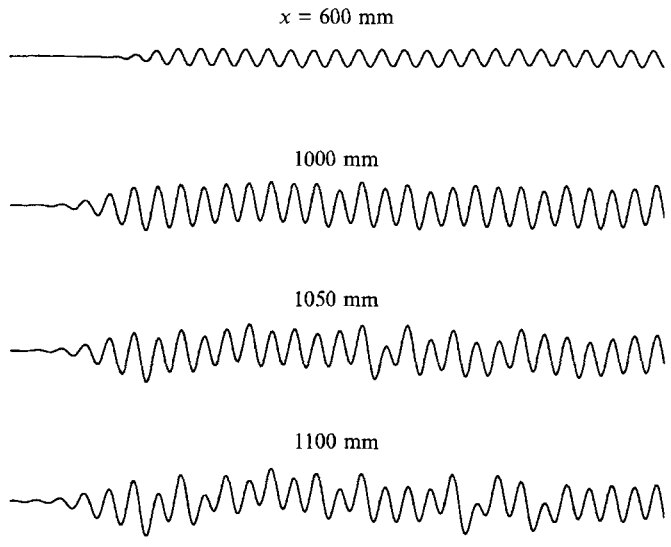


FIGURE 1. Hot-wire signals taken at different streamwise locations showing the progressive increase in complexity. They are all plotted with the same vertical scaling, and each has been shifted horizontally by the mean convection speed.

### 2.2. *Experimental procedure*

The experiment consisted of collecting hot-wire signals from various locations directly downstream from the source. All the hot-wire signals were obtained with the wire located at a non-dimensional distance $\eta = 1.5$ from the plate where $\eta = y(U/x\nu)^{\frac{1}{2}}$, $x$ is the distance from the leading edge, $y$ is the distance from the plate, $U$ is the free-stream velocity and $\nu$ is the kinematic viscosity of air. This value of $\eta$ corresponds to the strongest maximum of the Tollmien–Schlichting eigenfunction, i.e. the distance from the plate at which the amplitude of the Tollmien–Schlichting waves is greatest.

The hot-wire anemometer signals were recorded at 50 mm intervals from 300 mm to 1100 mm from the leading edge of the plate. At each station, sixty realizations were ensembled to improve the signal-to-noise ratio. This is possible because the signals are highly reproducible and so any random fluctuations due to background noise can be averaged out. The standard deviation of the different realizations was monitored to check that a satisfactory level of reproducibility was being maintained. The standard deviation is found to increase at the most downstream locations. This may be due either to the flow becoming more sensitive to the presence of small background disturbances, or perhaps to the existence of a multiplicity of final states which the solution can jump between. The latter possibility would be very intriguing but cannot be investigated with the present data since only the averaged data and the standard deviations were stored (saving individual realizations would have increased the data storage requirements sixty-fold).

### 2.3. *Experimental results*

The ensembled time series are close to a sinusoidal form over the upstream region of the plate, but further downstream the time series become increasingly modulated and complicated, see figure 1. There is a lag time at the beginning of each time series due to the time taken for disturbances introduced at the source to propagate to the measured position. By comparing the lag time for two adjacent positions it is possible to estimate the speed of propagation, which comes to 68 time steps or approximately

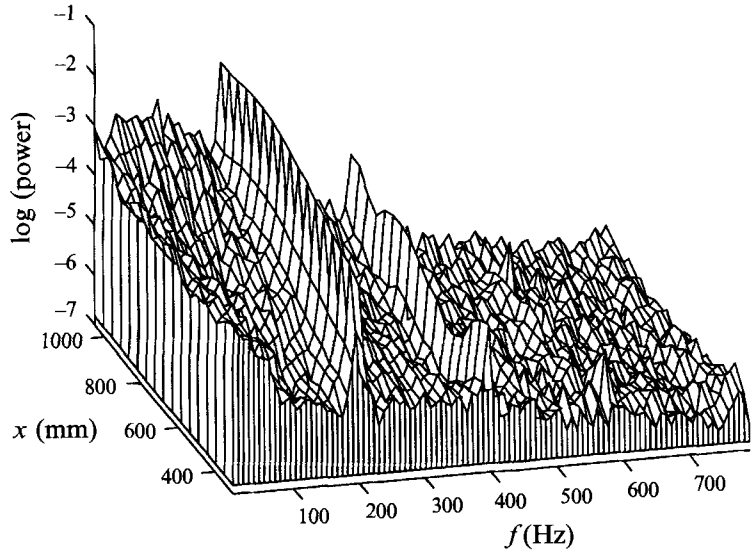


FIGURE 2. Isometric graph of power spectra over a range of streamwise locations showing the evolution of spectral components as the disturbance propagates downstream.

$0.33U$, comparing well with the linear stability results given in White (1974). This phase velocity is expected to have a slight variation in the streamwise direction as the boundary layer grows, but the effect is small over the region of interest. All the time series have been shifted relative to one another by 68 time steps. The residual movement to the left is a consequence of the dispersion of the initially sharp switch-on of the signal.

Power spectra of the records have been calculated at each $x$ position and are plotted as an isometric graph in figure 2. The calculations have been performed on the part of the time series after the lag time and where the oscillations are well established; the signal here is effectively stationary. The fundamental 200 Hz component is clearly visible and, in addition, the first harmonic and a subharmonic broadband appear. The harmonic component is not believed to be a consequence of any distortion in the instrumentation or filtering (M. Gaster 1993 personal communication). In figure 3 the linear stability of the frequency–Reynolds-number parameter space is shown. The frequency and Reynolds number are both made non-dimensional with respect to the boundary-layer displacement thickness:

$$\omega = \frac{1.72 \times 2\pi f}{U}\left(\frac{\nu x}{U}\right)^{\frac{1}{2}} \tag{1}$$

and

$$Re = 1.72\left(\frac{Ux}{\nu}\right)^{\frac{1}{2}}, \tag{2}$$

where $f$ is the frequency (measured in Hz) of the disturbance. The numerical factor follows from the assumption of a Blasius profile. Hence $\omega$ and $Re$ increase with distance from the leading edge. The region enclosed within the neutral stability curve NN′ is unstable, that outside is stable; this curve is taken from the tabulated values given in Jordinson (1970). A 200 Hz disturbance propagates along the ray AB shown in figure 3, and a 400 Hz disturbance propagates along the ray CD. The points A and C

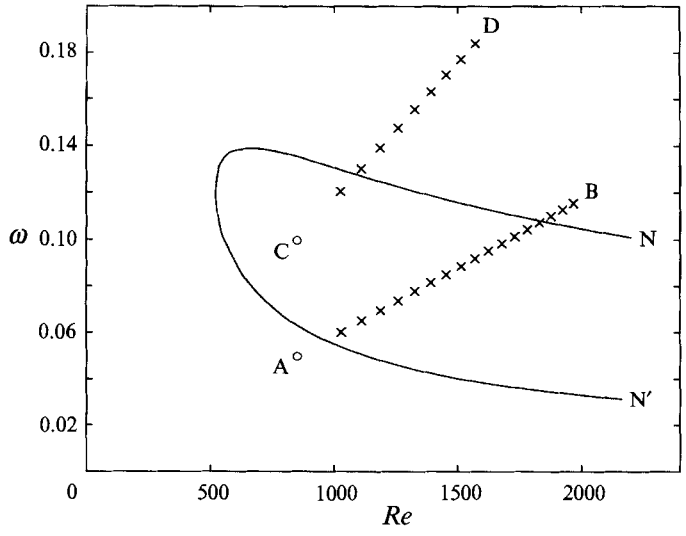


FIGURE 3. Stability map for steady flow over a flat plate. Dimensionless frequency is measured along the vertical axis, Reynolds number along the horizontal axis (both made dimensionless using the displacement thickness). The region within the neutral stability curve NN′ is unstable. AB and CD correspond to 200 Hz and 400 Hz disturbances respectively. Circles mark the location of the driving hole and crosses show the measurement stations.

correspond to the location of the driving hole, and the crosses correspond to the positions at which measurements were made.

The forcing mechanism may itself be nonlinear and so in addition to the fundamental 200 Hz signal, harmonics are also expected to be introduced into the boundary layer. At the driving hole, the linear theory predicts that the 200 Hz signal should decay while a 400 Hz signal should grow. However, at the first measuring sites, the fundamental 200 Hz signal should now be amplified, while the 400 Hz harmonic should decay. In the experiment, see figure 2, the 200 Hz signal can be seen to grow initially in amplitude, and the first harmonic, arising from nonlinear distortion at the driving hole, is observed to decay for the first few measurement stations. Thus the behaviour of the spectra for the signals captured nearest the leading edge are consistent with the linear theory.

Beyond the first few measurement positions, the first harmonic also starts to grow. This is clearly incompatible with the linear theory and must arise from the effects of nonlinearity in the fluid flow. Further downstream, the broadband component increases dramatically in amplitude.

## 3. Spatio-temporal data analysis

### 3.1. *The basic ideas*

Each data set is projected onto an optimally constructed phase space using the technique of Broomhead & King (1986) based on the 'method of delays', see Takens (1981). An $n$-window, which selects $n$ consecutive records from the time series, is passed along the data set to form $N$ $n$-dimensional position vectors. Singular value decomposition is then used to determine a basis which spans these position vectors. The SVD algorithm given in Press *et al.* (1986) was employed. A log-graph of the singular values and graphs of the first 10 singular vectors obtained from a typical hot-wire time series are shown in figure 4. An embedding window of $n = 20$ was used,

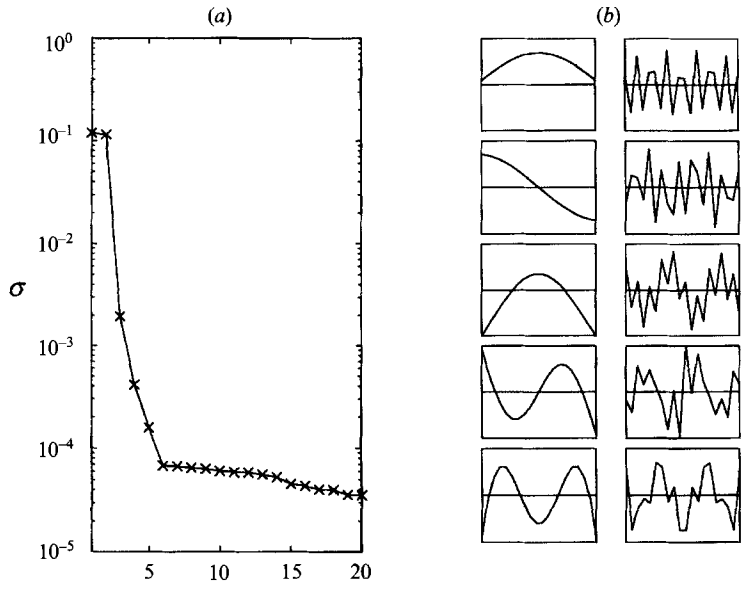


FIGURE 4. SVD of the trajectory matrix formed from the time series at 800 mm from the leading edge. The singular values are shown on a log plot in (*a*) and the first ten singular vectors in (*b*).

corresponding approximately to the first minimum of the autocorrelation function. There are a small number singular values significant above the noise, the first two are of almost equal energy and the corresponding singular vectors form a pair of sine and cosine waves. They have a period equal to twice the window length and hence correspond to the fundamental 200 Hz component of the signal which dominates both the autocorrelation function and the singular spectrum. The additional singular vectors have shapes reminiscent of successively higher order polynomials.

However, although the singular vectors give a set of linearly independent modes, some of these may have arisen from nonlinear interactions (analogous to harmonics in the Fourier spectrum). A new technique for estimating the energy in each mode that can be attributed to nonlinearity has been applied to this data set – for full details, see Healey (1993).

In that paper it is shown that if, say, the $(k+1)$th singular vector arises from nonlinearity then there exists a nonlinear function that relates the data projected onto this vector to the data projected onto the first $k$ singular vectors. The method involves fitting radial basis functions to test for possible nonlinear relationships among the singular vectors. Radial basis functions were developed as a convenient multi-dimensional interpolant, see Powell (1985). They have been used successfully to model the evolution on reconstructed attractors, see Casdagli (1989), enabling short-term prediction of chaotic time series. An important feature is that they can be used with irregularly distributed data points.

It is straightforward to extend the basic interpolation technique to give a least-squares fit. The interpolation (i.e. when the function passes through all the data points) involves inverting a square matrix. The least-squares fit is obtained by solving the over-determined problem posed by using more data points than free parameters. This is achieved using the singular value decomposition of the corresponding rectangular matrix (which is described more fully below).

However, in this application, it is not the evolution *on* the attractor that is to be

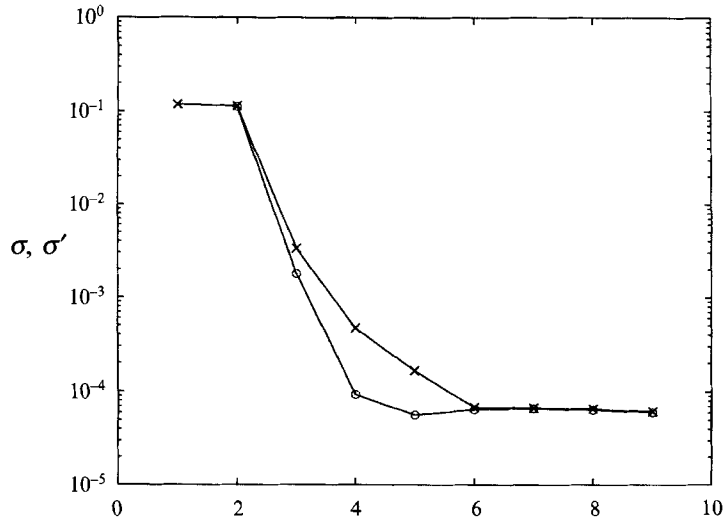


FIGURE 5. Comparison of singular values, $\sigma$ (crosses), and the energy remaining when nonlinear interactions are removed, $\sigma'$ (circles), on a log-scale for the data set in figure 4.

modelled, but the graph of the attractor projected on one singular vector versus the attractor projected onto the other singular vectors. The approach is to fit a large number of points on the attractor to a model with relatively few parameters (2000 points and 100 parameters has been used throughout). The standard deviation between the data points and the model, $\sigma'$, is then calculated and compared to the standard deviation of the data itself, $\sigma$, given by the corresponding singular value. The quantity $\sigma'$ is, effectively, the energy remaining in the mode after nonlinearity has been accounted for. In general, 2000 data points will only be well approximated by a 100-parameter model if the data are correlated and lie on a well-defined surface. This will be the case if the data projected onto one singular vector are a simple nonlinear function of the data projected onto the other singular vectors. The deviation between data and model will then be very much smaller than the deviation of the data along the chosen axis ($\sigma' \ll \sigma$). On the other hand, if $\sigma' \approx \sigma$ then the model is unable to detect any correlations among the data and no nonlinear dependence has been found among the singular vectors.

When this method is applied to the data of figure 4 the singular spectrum shown in figure 5 is obtained. The crosses show the singular values, $\sigma$, and the circles show the energy remaining after the nonlinearity has been removed, $\sigma'$, on a log scale.

It is now clear that there are only three truly independent modes – the fourth and fifth singular values are related to 'harmonics' in the spectrum. This conclusion can be confirmed by comparing the $\sigma$ and $\sigma'$ spectra as they evolve downstream. Figure 6(*a*) shows how the singular spectrum varies with streamwise position. The two most energetic singular values correspond to the fundamental forcing frequency and their growth is qualitatively similar to that of the fundamental in the Fourier spectrum, cf. figure 2. The fourth and fifth singular values ape the first harmonic in the Fourier spectrum, cf. figure 2. Figure 6(*b*) shows the spectra after nonlinearity has been accounted for. The first two are unchanged, but the fourth and fifth are almost completely suppressed over most of the plate. This is consistent with the interpretation of these singular values obtained from the analysis outlined briefly above. Further downstream a fourth mode emerges, and more would be expected yet further

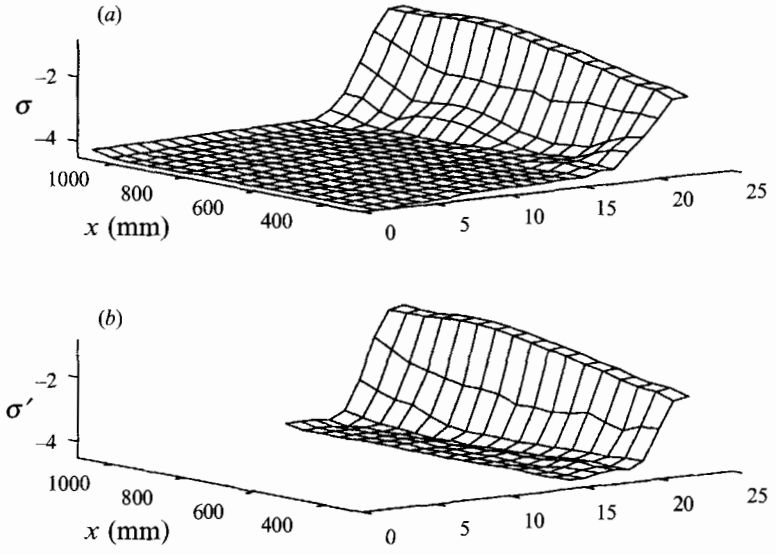


FIGURE 6. (*a*) Isometric graph of how the singular spectrum, $\sigma$, evolves in the streamwise direction. (*b*) Isometric graph of how the energy in the singular spectrum after the nonlinear interactions have been removed, $\sigma'$, evolves in the streamwise direction.

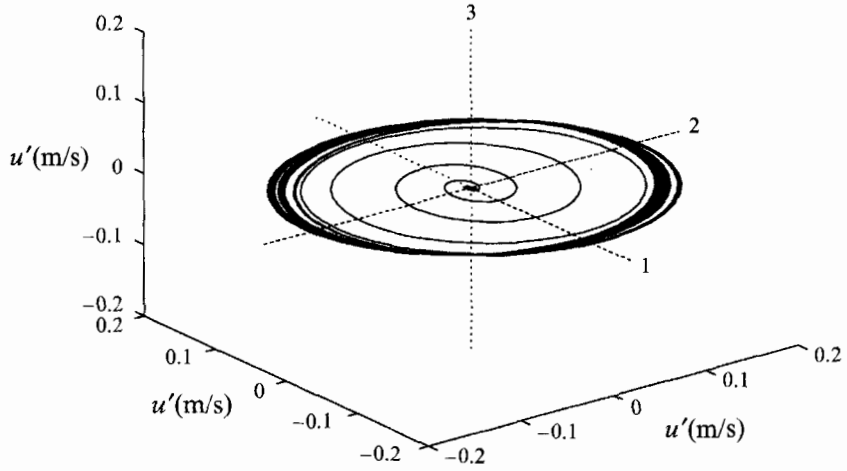


FIGURE 7. The reconstructed phase portrait projected onto the first three singular vectors for the data in figure 4.

downstream as transition progresses. However, for the purposes of this work, only the first three modes will be used to characterize the signals since the other modes are lost in the noise floor, see figure 6(*b*). This approximation is expected to break down for the most-downstream data sets, but to be adequate for the rest.

The phase portrait, projected onto the first three singular vectors is shown in figure 7. Initially the trajectory is confined to a small neighbourhood near the origin of the phase space – this corresponds to the section of the time series measured before the disturbance introduced by the loudspeaker is convected downstream to the hot-wire probe. There follows a period of spiralling growth as the leading edge of the disturbance sweeps past the probe, followed by a basic circulating motion due to the nearly sinusoidal nature of the time series.

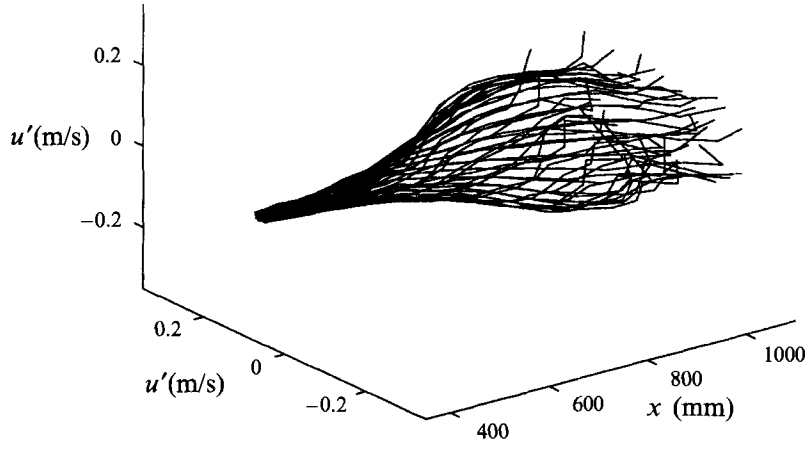


FIGURE 8. Augmented phase space showing the spatio-temporal evolution of disturbances.

The irregular modulation of the sine waves causes the thickening of the phase portrait and makes it (at least) three-dimensional. Hence the third singular value may be taken to correspond, in some sense, to the subharmonic component of the Fourier spectrum. This modulation can be traced back to the random numbers added to the fundamental sine wave to form the original forcing data. Thus the evolution is not deterministic in time in the sense that the future dynamics cannot be predicted from a knowledge of the previous history. For example, the onset of spiralling in figure 7 cannot be predicted from the initial section of time series.

Nonetheless, the evolution is deterministic in a spatial sense – a knowledge of the time history at an upstream location is sufficient to predict, for example, the onset of spiralling at some downstream location (provided the flow is two-dimensional and that a suitable convection time can be found). This corresponds to following the disturbance in the $(x, t)$ plane rather than considering vertical slices (time series) which intersect the disturbances.

Therefore, instead of studying a single phase portrait as in figure 7, it is proposed that the whole set of phase portraits from all the measurement stations should be incorporated in an 'augmented phase space' where the position, $x$, of the probe is treated as an additional dimension. In this augmented space a data point on one reconstructed phase portrait is connected to its corresponding point on its neighbouring downstream portrait. Thus a flow which evolves in $x$ is generated, see figure 8.

In this augmented phase space, $x$ plays the role normally associated with time, $t$, i.e. the independent variable, and at the most-upstream measurement point $x_0$, $t$ generates a series of 'initial conditions', i.e. a set of points each of which is propagated downstream by the flow.

Phase portraits taken from positions near the excitation source appear at the lower left-hand end whereas the portraits from far downstream locations appear at the upper right-hand end of the diagram. The exponential growth in space predicted by linear theory is clearly visible in the initial stage. As $x$ increases further, however, the amplitude of the motion is seen to saturate. This can also be explained by linear theory because the boundary layer grows in thickness, and, as discussed in §2.3, the Reynolds number and frequency are made dimensionless with respect to the boundary-layer displacement thickness, and so they too increase as $x$ increases leading to changing growth rates.

The fact that the modal selection process varies with streamwise position in a non-parallel boundary layer must be incorporated in any modelling scheme. A piecewise approach, in which the boundary layer is decomposed into a number of sections, each one delimited by the measurement stations on either side may thus be a suitable choice. Each section is modelled individually, and a chain of models can then be built up to describe the spatio-temporal evolution of the disturbance over the whole boundary layer. The model parameters are expected to vary smoothly with $x$, reflecting the smooth increase in boundary-layer thickness.

It is assumed that a map $\Phi_n$ can be found which will transform the set of points $\{y_i\}$ on a portrait at position $x_n$ to the set of points $\{y'_i\}$ on the portrait taken at $x_{n+1}$:

$$y'_{i+k} = \Phi_n(y_i), \tag{3}$$

where $y'_{i+k}, y_i, \Phi_n \in \mathscr{R}^m$, $m$ is the number of significant singular vectors used in the embedding (here $m = 3$) and $k$ is a suitable delay allowing for the time taken for the disturbance to convect from $x_n$ to $x_{n+1}$ (here $k = 68$). The $j$th element of $\Phi_n$, $\Phi_{nj}$, is composed of a sum of $p$ basis functions $b_l(y_i)$:

$$\Phi_{nj}(y_i) = \sum_{l=1}^{p} \omega_{lj}\, b_l(y_i) \tag{4}$$

and the weights, $\omega_{lj}$, are chosen to minimize

$$\sum_{i=1}^{N} \|y'_{i+k} - \Phi_n(y_i)\|^2, \tag{5}$$

where $\|\cdot\|$ denotes the Euclidean norm. This least-squares solution can be readily obtained by casting the problem in matrix form and using singular value decomposition. The $N$ known values of $y'_{i+k}$ and $y_i$ are substituted into (3) and (4) and the resulting $N$ simultaneous equations expressed as

$$\underbrace{\boldsymbol{Y}'}_{N\times m} = \underbrace{\boldsymbol{B}}_{N\times p}\,\underbrace{\boldsymbol{\Omega}}_{p\times m}, \tag{6}$$

where the $i$th row of $\boldsymbol{Y}'$ is given by the transpose of $y'_{i+k}$, the element $B_{il}$ is given by $b_l(y_i)$ and the elements of $\boldsymbol{\Omega}$ are the weights $\omega_{lj}$. The least-squares solution to (6) is given by

$$\boldsymbol{\Omega} = \boldsymbol{B}^{+}\boldsymbol{Y}', \tag{7}$$

where $\boldsymbol{B}^{+}$ is the left inverse of $\boldsymbol{B}$ and is calculated from its singular value decomposition:

$$\boldsymbol{B} = \boldsymbol{S}\boldsymbol{\Sigma}\boldsymbol{C}^{T} \Rightarrow \boldsymbol{B}^{+} = \boldsymbol{C}\boldsymbol{\Sigma}^{-1}\boldsymbol{S}^{T}. \tag{8}$$

The decomposition yields three matrices $\boldsymbol{S}$, $\boldsymbol{\Sigma}$ and $\boldsymbol{C}$ where $\boldsymbol{S}$ and $\boldsymbol{C}$ are orthonormal and contain the left and right singular vectors of $\boldsymbol{B}$ and $\boldsymbol{\Sigma}$ is diagonal and contains the (non-negative) singular values $\sigma_i$. If $\boldsymbol{B}$ is singular then $\boldsymbol{\Sigma}^{-1}$ is replaced by the diagonal matrix $\boldsymbol{\Sigma}^{+}$ whose elements are given by

$$\sigma_i^{+} = \begin{cases} \sigma_i^{-1} & \text{if } \sigma_i \neq 0 \\ 0 & \text{if } \sigma_i = 0. \end{cases} \tag{9}$$

When analysing experimental data, $\boldsymbol{B}$ will never be singular, but it may be ill-conditioned, so it is necessary to introduce a level of tolerance, $\epsilon$, and use

$$\sigma_i^{+} = \begin{cases} \sigma_i^{-1} & \text{if } \sigma_i > \epsilon \\ 0 & \text{if } \sigma_i < \epsilon. \end{cases} \tag{10}$$

The use of (10) instead of (9), implying that $\boldsymbol{B}$ has rank $r$ (i.e. $r$ singular values greater than $\epsilon$), means that the data only support the use of $r$ rather than $p$ independent parameters (for the basis $b_l$ chosen). In this case SVD arranges that $p-r$ of the parameters are linearly dependent on one another.

### 3.2. *Linear modelling*

It is informative to consider the case of a linear model for $\Phi$ since this can be related to standard spectral methods. The basis functions $b_l$ are then simply the components of $\boldsymbol{y}_i$:

$$b_l(\boldsymbol{y}_i) = y_{il}, \tag{11}$$

where $y_{il}$ is the $l$th component of the position vector $\boldsymbol{y}_i$. Hence $\boldsymbol{B}$ of (6) has the same structure as $\boldsymbol{Y}'$, so, let $\boldsymbol{Y} = \boldsymbol{B}$. When the embedding window is very large, each embedding vector contains an approximately stationary section of time series, in which case the proper orthogonal theorem (which underpins SVD) reduces to the harmonic orthogonal decomposition theorem (see Lumley 1981). Thus the singular vectors are now harmonic bases and the singular values are the magnitudes of the Fourier components. Now let the embedding window have the same length as the time series. $N$ embedding vectors (each of dimension $N$) can be constructed by wrapping the end of the time series onto its beginning (using the stationarity of the time series). Let $\boldsymbol{X}$ and $\boldsymbol{X}'$ be the trajectory matrices so constructed for two time series taken from neighbouring measurement stations in the boundary layer. $\boldsymbol{X}$ and $\boldsymbol{X}'$ are symmetric Toeplitz matrices and their singular values are equal to their eigenvalues and their singular vectors are equal to their eigenvectors (this is true for any symmetric matrix). Moreover, since these eigenvectors are equivalent to a Fourier basis, the eigenvectors of $\boldsymbol{X}$ and $\boldsymbol{X}'$ are equal to one another, and so

$$\boldsymbol{X} = \boldsymbol{S}\boldsymbol{\Sigma}\boldsymbol{C}^T = \boldsymbol{U}\boldsymbol{\Lambda}\boldsymbol{U}^T \tag{12}$$

and

$$\boldsymbol{X}' = \boldsymbol{S}'\boldsymbol{\Sigma}'\boldsymbol{C}'^T = \boldsymbol{U}\boldsymbol{\Lambda}'\boldsymbol{U}^T, \tag{13}$$

where $\boldsymbol{U}$ are the eigenvectors (Fourier bases) and $\boldsymbol{\Lambda}$ and $\boldsymbol{\Lambda}'$ are the eigenvalues (Fourier coefficients) of $\boldsymbol{X}$ and $\boldsymbol{X}'$ respectively. The matrices $\boldsymbol{Y}$ and $\boldsymbol{Y}'$ are obtained by projecting the Toeplitz matrices $\boldsymbol{X}$ and $\boldsymbol{X}'$ onto their eigenvectors: $\boldsymbol{Y} = \boldsymbol{X}\boldsymbol{U}$ and $\boldsymbol{Y}' = \boldsymbol{X}'\boldsymbol{U}$, and thus (6) becomes

$$\boldsymbol{X}'\boldsymbol{U} = \boldsymbol{X}\boldsymbol{U}\boldsymbol{\Omega}. \tag{14}$$

Substituting (12) and (13) and (14), and using the orthonormality of $\boldsymbol{U}$ the following expression is obtained:

$$\boldsymbol{\Omega} = \boldsymbol{\Lambda}^{-1}\boldsymbol{\Lambda}'. \tag{15}$$

This result demonstrates that the linear map $\boldsymbol{\Omega}$ which transforms the data from one $x$ station to the next is a diagonal matrix whose elements are the quotients of the Fourier coefficients of each of the two original time series.

Therefore, in the limit of long embedding windows, if a linear model is chosen for $\Phi$ in (4) the resulting map is the same as the one that would be obtained by simply dividing the Fourier transform of one series by the Fourier transform of the other (although the phase information is lost in this process – in this derivation the relative phases are assumed unchanged).

This rather loose argument should not be regarded as a 'proof' but serves to illustrate the relationship between the formulation of (3) and more familiar techniques.

When $m$ and $n$ are relatively small (and the elements within the embedding windows

are non-stationary), then the linear model equation (3) can be regarded as a 'low-dimensional' analogue to conventional spectral techniques. This is not the same as filtering out low-energy spectral components since the SVD bases are not harmonics. Instead, SVD gives the lowest dimensional basis optimized with respect to energy. Thus the eigenvalues of $\boldsymbol{\Omega}$ (which in general is not diagonal for small $m$) give the stability of the 'major features' of the flow, rather than of any particular spectral components.

The attraction of (3) is the ease with which the analysis can be extended to nonlinear models and its classical low-dimensional dynamical systems formalism.

### 3.3. *Nonlinear modelling*

It shall be assumed that for measurement stations that are sufficiently close to one another, the evolution of the flow may be modelled by quadratic basis functions in addition to the linear terms of the form (11):

$$b_l(x) = x_i x_j, \tag{16}$$

where $x$ is some vector, $x_i$ one of its components and $i$ and $j$ vary to generate all possible quadratic combinations. It might be assumed (naively) that for sufficiently close measurement stations purely linear models could be used, but the cumulative effect of many linear models is still a linear model, while the cumulative effect of a number of quadratic models is a highly nonlinear model (cf. Feigenbaum's 1-D map). This is crucial for the proper modelling of transition. In this work, the model contains both linear and quadratic terms.

The method of §3.1 can now be implemented, but there remains a difficulty. It is not known *a priori* what rank $r$ should be given to $\boldsymbol{B}$, i.e. what level $\epsilon$ should take in (10). For example, if the flow is genuinely evolving according to linear relationships, as is the case for sufficiently small-amplitude disturbances, then the quadratic bases will be superfluous and $r$ could be chosen to utilize only the linear terms. Further downstream, the evolution may be strongly quadratic and $r$ should be larger to accommodate the quadratic terms, but even then, not all of the quadratic terms may be appropriate.

Our formula for choosing a value for $r$ is as follows. Instead of using all $N$ vectors $\{\boldsymbol{y}_i'\}$ and $\{\boldsymbol{y}_{i+k}\}$ in (6), use only alternate points. The remaining points can then be used to test the efficacy of the model – an r.m.s. error can be calculated which measures the accuracy of predictions made of unseen data points. The procedure is repeated for a range of values of $r$, and the one which makes the most accurate predictions is chosen. Construction of $B$ and its singular value decomposition only have to be performed once, and only the weights and r.m.s. errors have to be recalculated.

## 4. Application to experimental data

Quadratic three-dimensional maps have been fitted to the data sets discussed in §2.3. The rank of each model has been chosen in accordance with the method outlined at the end of §3.3. The behaviour of small-amplitude disturbances are characterized by the eigenvalues of the nonlinear maps linearized at the origin of phase space. These eigenvalues have been calculated using an algorithm from Press *et al.* (1986). The eigenvalues give the behaviour of the dominant flow features ('modes') and cannot in general be identified with particular spectral components. It is convenient to consider the natural logarithms of the eigenvalues – then positive real parts correspond to exponentially growing modes and negative real parts correspond to exponentially

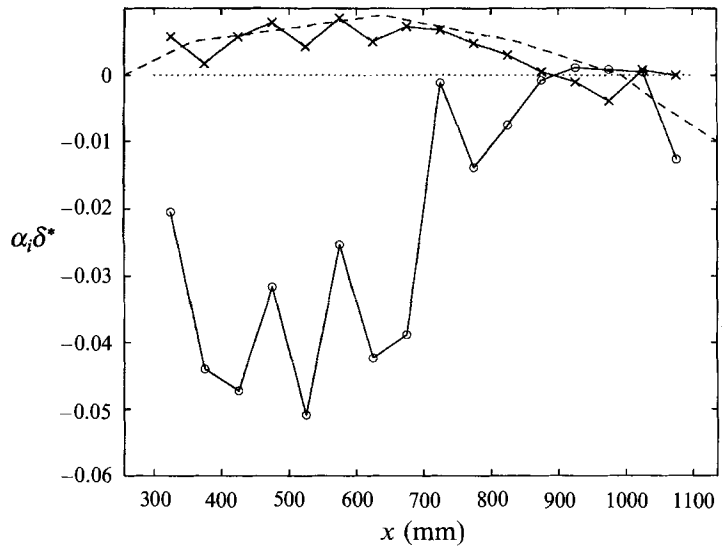


FIGURE 9. $x$-dependence of the growth rates (non-dimensionalized with respect to boundary-layer displacement thickness) estimated from the eigenvalues of the fitted maps linearized at the origin. The crosses correspond to the fundamental frequency component, the circles correspond to the component associated with the subharmonic band and the dashed line gives the results for the fundamental frequency from linear stability analysis.

decaying modes. These spatial growth rates are then non-dimensionalized with respect to the local boundary-layer displacement thickness for comparison with linear theory.

A graph of the real part of the eigenvalues versus $x$ position is shown in figure 9. The horizontal dotted line represents neutrally stable modes. For most of the range there is a complex-conjugate pair and one real eigenvalue. Complex eigenvalues represent a phase shift. From figure 4 it is apparent that the flow is largely dominated by a pair of singular vectors corresponding very closely to the fundamental Fourier component of the forcing, and the complex-conjugate pair of eigenvalues can be associated with these modes. The real part of this pair is initially positive, increases to a maximum and then passes through zero further down the plate, ultimately becoming negative.

This behaviour is consistent with the linear theory shown in figure 3, i.e. the mode is unstable, but with a growth rate which increases to a maximum (as the ray AB approaches the centre of the neutral stability curve) then decreases, finally becoming negative (after the ray AB has crossed the neutral stability curve). The fact that it has an imaginary part is due to the delay $k$ in (3), which can only take integer values, not exactly coinciding with the group velocity of the disturbance (causing a small phase shift between neighbouring maps). There is quantitative agreement between the growth rate of the fundamental frequency predicted by linear theory (from White 1974, dashed line) and those estimated using the method of §3 (crosses).

The third eigenvalue is strongly negative over the upstream part of the plate but becomes much closer to zero further downstream. This eigenvalue could be interpreted as representing the gross behaviour of the subharmonic band in the power spectrum – which is the next most dominant feature after the fundamental component. It is clear from figure 3 that rays corresponding to low-frequency disturbances will be stable upstream and only destabilize sufficiently far downstream. Further down the plate the third eigenvalue becomes positive (eventually low-frequency rays will cross the lower branch of NN′ in figure 3) while the complex pair become negative giving a saddle

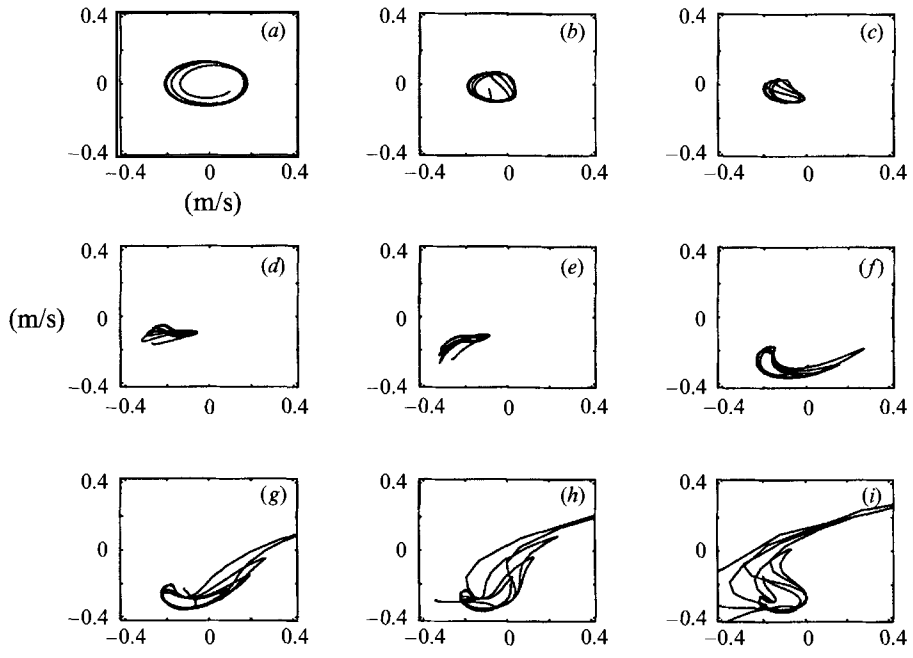


FIGURE 10. Series of iterates of one of the fitted maps (using an experimental data set for the initial points). The stretching and folding are reminiscent of Smale horseshoe maps, and suggest sensitive dependence on initial conditions. $x = 900$ mm.

point in the augmented phase space. This reflects the fact that some frequencies are unstable while others are stable. A three-dimensional space is the smallest in which this sort of saddle-focus fixed point can exist, but it does capture the basic dynamics of the flow (which itself is infinite-dimensional).

An effect of nonlinearity is that the behaviour away from the origin need not be the same as that near the origin, i.e. larger disturbances can evolve differently from small disturbances (as is known to be the case in transition). In addition, there exists the possibility that more exotic types of behaviour may be present, for example a Smale horseshoe map in which repeated stretching and folding lead to sensitive dependence on initial conditions and the possibility of chaos (as in the Henon map, see Guckenheimer & Holmes 1986). Horseshoe maps can also be generated by homoclinic orbits (see Wiggins 1988), and our saddle focus could potentially give rise to homoclinicity.

Having deduced a set of maps, each corresponding to different locations in the boundary layer, it is interesting to pick one, for instance far enough down the plate to give maps with three eigenvalues of the same magnitude, and to iterate it to see what it does. Figure 10 shows a series of snapshots obtained by iterating one of the maps many times. There appears to be evidence for stretching and folding but since the points diverge after a fairly small number of steps it is difficult to derive firm conclusions (points in the standard Smale horseshoe map also diverge).

It may be possible to construct more robust maps if say two different data sets, measured when different forcing amplitudes were used, are combined to deduce the models. In this way a greater volume of phase space would be explored and the nonlinear terms would be better supported. Nonlinear modelling of the impulse response for a range of excitation amplitudes could be studied and also the role of three-dimensional flow effects.

## 5. Conclusions

A series of experiments has been performed in which the boundary layer was excited by a loudspeaker and its response was measured at a number of regularly spaced streamwise positions. The resulting time series are projected onto optimally constructed phase spaces, and then linked together using the $x$-coordinate of the measurement position as an additional dimension. A new technique for estimating the number of independent modes has been applied and shows that only three phase space dimensions are needed to describe these data sets. In this way the spatio-temporal evolution of disturbances can be studied. Nonlinear maps have been fitted to the data to model the spatial growth of the signal. The properties of these maps are consistent with classical linear stability theory for small-amplitude disturbances, and at larger amplitudes give rise to more complicated dynamics involving the stretching and folding of phase space. We believe that this is the first time that this behaviour has been deduced from experimental 'open flow' fluid data.

The method explicitly incorporates non-parallel effects and the inherent convective nature of the boundary layer. For this reason it may be applicable to many other types of shear-layer flows. Research is now being carried out to investigate the results of using different sorts of forcing to drive the loudspeaker, and to assess its potential to act as a general boundary-layer predictor.

This work has benefitted from the discussions with Professor Gaster and other members of the Transition Research Group in the Cambridge University Engineering Department. The author was supported by the SERC (UK).

## REFERENCES

BROOMHEAD, D. S. & KING, G. P. 1986 Extracting qualitative dynamics from experimental data. *Physica D* **20**, 217–236.

CASDAGLI, M. 1989 Nonlinear prediction of chaotic time series. *Physica D* **35**, 335–356.

GASTER, M. 1962 A note on the relation between temporally-increasing and spatially-increasing disturbances in hydrodynamic stability. *Phys. Rev. Lett.* **59**, 845–848.

GASTER, M. 1990 The nonlinear phase of wave growth leading to chaos and breakdown to turbulence in a boundary layer as an example of an open system. *Proc. R. Soc. Lond.* A **430**, 3–24.

GUCKENHEIMER, J. & HOLMES, P. 1986 *Nonlinear Oscillators, Dynamical Systems and Bifurcations of Vector Fields*, 2nd edn. Springer.

HEALEY, J. J. 1993 Identifying finite dimensional behaviour from broadband spectra. *Phys. Lett.* A (submitted).

HUSSAIN, A. K. M. F. 1986 Coherent structures and turbulence. *J. Fluid Mech.* **173**, 303–356.

JORDINSON, R. 1970 The flat plate boundary layer. Part 1. Numerical integration of the Orr–Sommerfeld equation. *J. Fluid Mech.* **43**, 801–811.

LUMLEY, J. L. 1981 Coherent structures in turbulence. In *Transition and Turbulence* (ed. R. E. Meyer), pp. 215–242. Academic.

POWELL, M. J. D. 1985 Radial basis functions for multivariable interpolation: A review. *Proc. IMA Conf. on Algorithms for the Approximation of Functions and Data.* RMCS Shrivenham, UK.

PRESS, W. H., FLANNERY, B. P., TEUKOLSKY, S. A. & VETTERLING, W. T. 1986 *Numerical Recipes.* Cambridge University Press.

TAKENS F. 1981 Detecting strange attractors in turbulence. In *Dynamical Systems and Turbulence*, Lecture Notes in Mathematics, vol. 898 (ed. D. A. Rand & L.-S. Young), p. 366. Springer.

WHITE, F. M. 1974 *Viscous Fluid Flow.* McGraw-Hill.

WIGGINS, S. 1988 *Global Bifurcations and Chaos.* Springer.